

Automated, non-metallic measurement facility for testing and development of electromagnetic induction sensors for landmine detection

Gregg D. Larson^{*} and Waymond R. Scott, Jr. [†]

^{*}Woodruff School of Mech. Eng., Georgia Institute of Technology, Atlanta, GA, USA 30332-0405

[†]School of Elec. and Comp. Eng., Georgia Institute of Technology, Atlanta, GA, USA 30332-0250

ABSTRACT

For development of electromagnetic induction (EMI) sensors for landmine detection, a testing facility has been established for automated measurements of typical targets with both individual sensors and arrays of sensors. A six-degree of freedom positioner has been built with five automated axes (three translational stages and two rotational stages) and one manual axis for target characterizations with no metal within the measurement volume. Translational stages utilize commercially-available linear positioner hardware. Rotational stages have been customized using non-metallic components to position the targets within the measurement volume. EMI sensors are held fixed in one location while the positioner orients the targets and moves them along a prescribed path through the region surrounding the sensor. The automated movement is computer-controlled and data are acquired continuously. Data are presented from three-dimensional scans of targets at various orientations. Typical targets include shell casings, wire loops, ball bearings, and landmines.

Keywords: Electromagnetic induction, EMI, landmine, detection, sensor, testing

1. INTRODUCTION

To detect the presence of landmines buried in soil, an electromagnetic induction (EMI) sensor has been developed and tested at multiple field locations¹⁻². Figure 1(a) shows a single broadband EMI sensor while Figure 1(b) shows a broadband array of EMI sensors, both at field locations. Both sensors were scanned close to the soil surface to detect buried targets. Details of the EMI sensor and its field testing can be found in the literature.

Sample data from field measurements of four anti-personnel landmines at various depths are shown in the Argand diagrams in Figure 2. The imaginary part of the response is graphed as a function of the real part with frequency as a parameter on the Argand diagrams. Each figure shows one type of target with responses plotted for different burial depths. The characteristic responses from the buried targets shown in Figure 2 are a function of the metal content and structure of the individual targets. Note that the shape of the response is consistent for each target and is insensitive to the burial depth. This shape information can be used to help discriminate between landmines and clutter³⁻⁷. However, little is known about how landmines and complex clutter objects behave when they are tilted at odd angles which could cause missed detections. To aid in the development of the EMI sensors and associated detection algorithms, a testing facility has been built to characterize the response of typical targets and clutter objects with respect to location and orientation. The data from these measurements will be used to study the response of the targets as a function of location and orientation. This type of measurement would be very difficult to perform in the field due to the difficulty of accurately placing and rotating the target. It is envisioned that the results of this work can be utilized to reduce false alarm rates and increase the probability of detection for EMI sensors through improvements in both the hardware and the processing algorithms used to detect and discriminate buried targets.

In the following sections, the testing facility will be described and experimental measurements will be shown along with theoretical results for representative targets including a single wire loop, three mutually orthogonal wire loops, and a 9 mm shell casing.

^{*} E-mail: gregg.larson@me.gatech.edu, Tel: 404-894-6026

[†] E-mail: waymond.scott@ece.gatech.edu, Tel: 404-894-3048



Fig. 1. Field measurement systems using (a) a single broadband EMI sensor and (b) an array of three broadband EMI sensors.

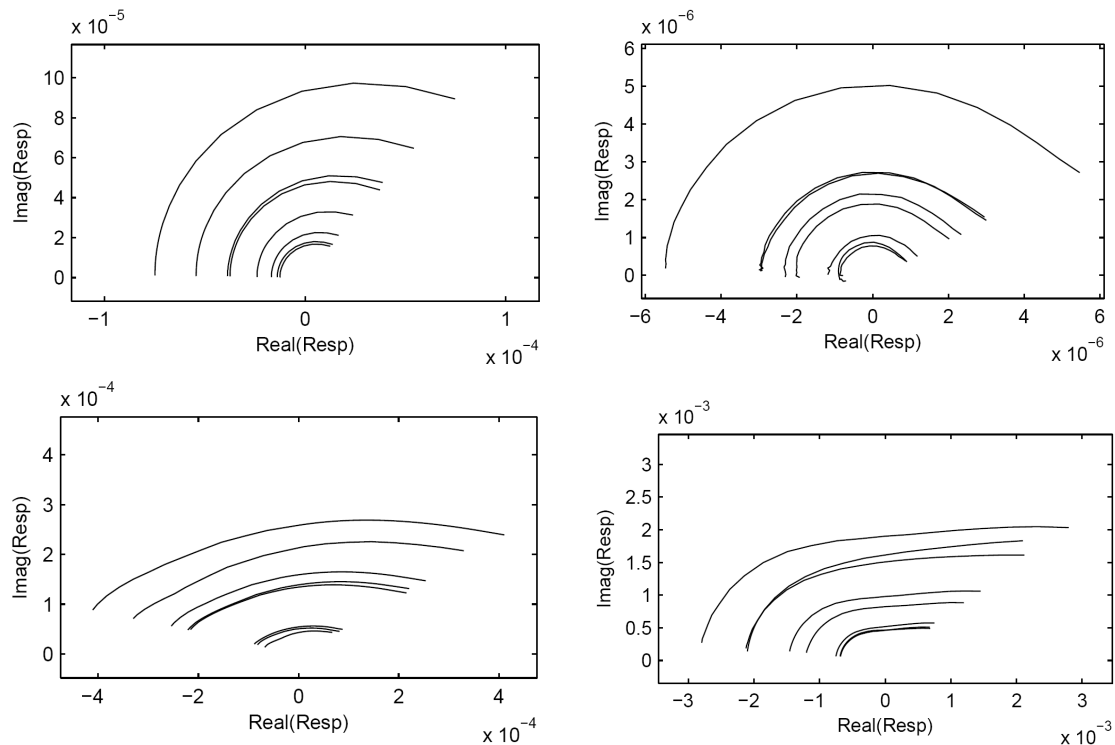


Fig. 2. Sample field data from four types of anti-personnel landmines presented in Argand diagrams. Each curve in figures (a) through (d) represents the response of a single target as a function of interrogation frequency. The response of multiple targets are shown in (a) through (d) with the amplitude differences between curves indicating targets with different burial depths.

2. EXPERIMENTAL FACILITY FOR CALIBRATION MEASUREMENTS

To measure the characteristic response of EMI sensors of several representative targets, a laboratory positioner was developed with three automated translational stages (x , y , and z), two automated rotational stages (yaw and pitch), and one manually-adjusted rotational stage (roll, not labeled) as indicated in Figure 3. A single EMI sensor is shown in Figure 3(b) with a single wire loop as the target while an array of three EMI sensors is shown in Figure 3(c) with a target that consists of three mutually orthogonal loops of different gauge wire. This system has been used to measure the response of targets in a three-dimensional region as a function of angular orientation. Other typical targets include shell casings, ball bearings, coplanar wire coils, and landmines.

The translational stages were built using commercially-available hardware including stepper motors, gear reducers, belts, and aluminum structural beams. The positioner can translate each target throughout a 2 m by 1 m by 0.5 m volume. The first automated rotational stage utilizes a Velmex rotary positioner (Model # B4818TS) with a stepper motor to control the yaw angle throughout a 360° range of motion. The second automated rotational stage was custom-built using fiberglass structural beams, polycarbonate connectors, fiberglass shafts, acetal/nylon/glass nonmetallic bearings, nylon miter gears, fiberglass-reinforced nylon sprockets, Delrin chains, and nylon bolts. A stepper motor controls the pitch angle throughout a 360° range of motion. The second rotational stage holds each target 70 cm from the nearest metal on the moving support beam. This second rotational stage is reconfigurable as the fiberglass structural beams can be replaced by different length beams to adjust to different size targets; this would also necessitate appropriate adjustments to the chains and fiberglass shafts.

The EMI sensor or array of EMI sensors is positioned in the middle of the measurement region, sufficiently distant from the floor (and its structural steel) and the aluminum beams of the positioner frame to minimize the measured response from the surrounding metal structures. Additionally, the response from the surrounding metal structures is subtracted from the measurements of the individual targets as a part of the EMI sensor's processing algorithms. While the EMI sensor is held fixed, the positioner orients the target in yaw and pitch and then translates it along a prescribed path computed by the data acquisition and motion control system. The path is continuous in the x direction with a discrete set of values for y and z . The path is repeated for each set of yaw and pitch angles.

The EMI sensor and the array of EMI sensors includes a surrounding coil that transmits an excitation signal. A multi-sine signal, composed of 21 distinct frequencies logarithmically spaced from 300 Hz to 90 kHz, is transmitted cyclically. The multi-sine signal has been optimized in regards to phase angle and amplitude as well as to minimize interference with power line harmonics. This cyclic transmission allows for continuous data acquisition in the time domain at 204 kSamples/second from each sensor with processing while the target is in motion. The time-domain data are transformed into the frequency domain using a fast Fourier transform. This operation is performed in real time and only the 21 complex-valued samples in the frequency domain for each measurement point are saved. This provides a substantial benefit in that the saved data can be reduced from 20,400 single-valued samples in the time domain to 21 complex-valued samples.

Continuously sampled data are acquired, processed, and saved at 0.1 second intervals while the target is in motion along the prescribed path. With the target moving at 4 cm/second in the x -direction, data are acquired every 0.4 cm along the x -axis. The data are then interpolated to 0.5 cm intervals for an evenly-spaced grid in the post-processing. As data are acquired at distinct y and z values, interpolation is not required in those dimensions.

A typical measurement for the EMI sensor array scans a target continuously from -51 cm to 51 cm in the x -direction and discretely at y -values from -30 cm to 30 cm in 10 cm increments and z -values from 0 cm to 22 cm in 1 cm increments for three yaw angles (0, 45, and 90 degrees) and five pitch angles (0, 22.5, 45, 67.5, and 90 degrees) over a 19 hour time period. Processing of the acquired data results in 30,581,145 complex data points. This is so much data that it is difficult to inspect it.

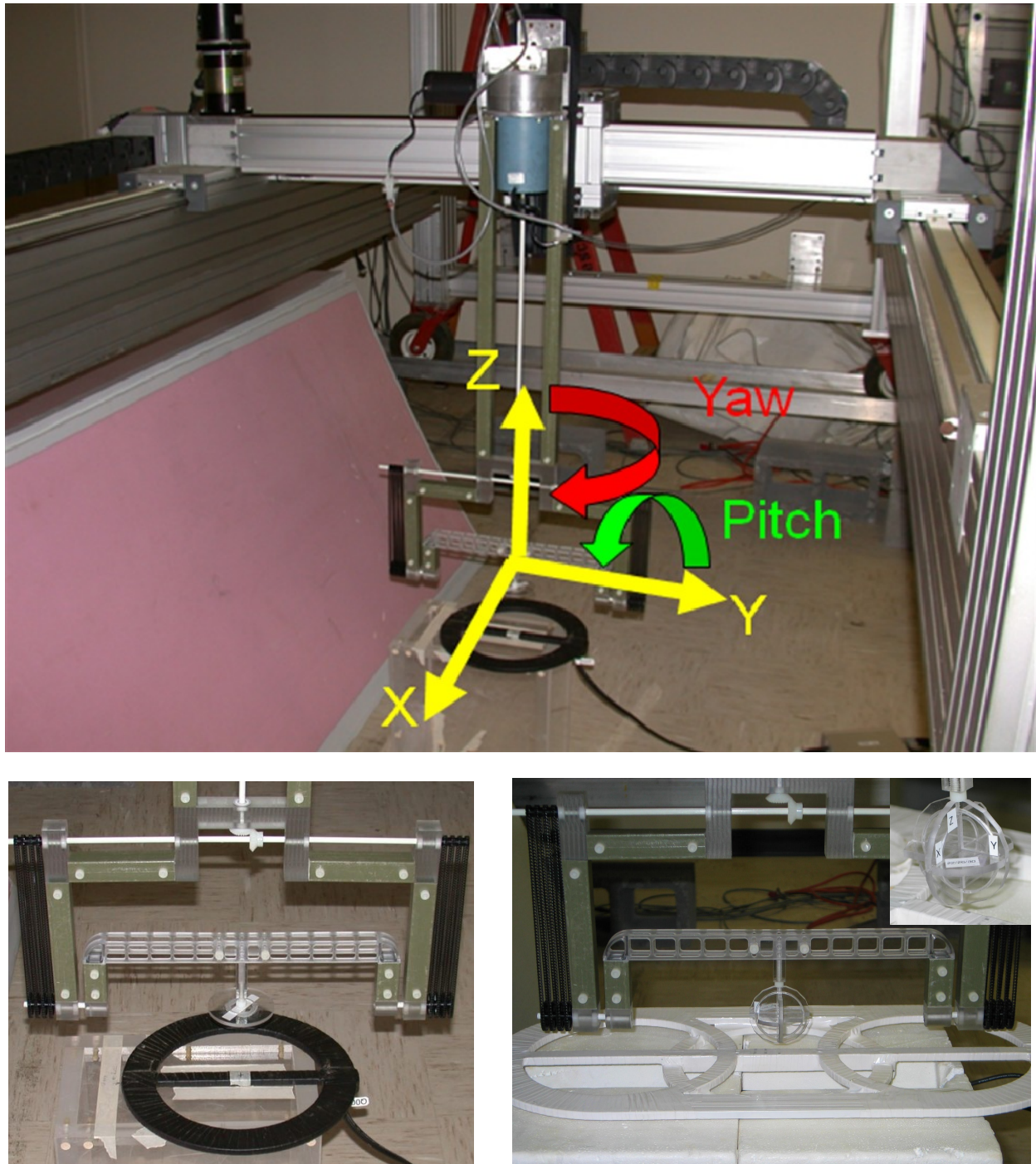


Fig. 3. Experimental measurement facility for EMI target characterization: (a) Automated translational (x , y , and z) and rotational (yaw about z and pitch about y) axes labeled, manual rotational (roll about x) axis not labeled; (b) Single wire loop target shown above single EMI sensor; and (c) Three mutually-orthogonal wire loops target (in inset photograph) shown above EMI sensor array (three EMI sensors).

3. EXPERIMENTAL AND NUMERICAL MEASUREMENTS

Measurements have been conducted of several typical EMI targets including landmines, shell casings, ball bearings, single wire coils, multiple coplanar wire coils, and three mutually orthogonal wire coils. Some targets are included due to practical interests in detection of the targets in the field while some are included for research and development of the EMI sensor hardware. All of the targets are of interest for detection and processing algorithm development efforts. Data from three targets (a single wire loop, a composite target with three mutually orthogonal wire loops, and a 9 mm shell casing) will be presented in this section; the wire loop targets are useful for demonstrating the EMI system performance capabilities while the shell casing has inherent practical interest and a comparatively simple response.

The measured data are filtered in the down-track direction by convolving the measured data with the zero-mean template shown in Figure 4. The filter is used to make the data from the measurement system directly comparable to that of the field systems in which the filter has three beneficial effects. First, it mostly removes the ground response by differencing closely located portions of the ground. Second, it mostly removes the drift in the system by differencing measurements made only a short time apart. Third, it averages the data over several locations which will improve the signal to noise ratio.

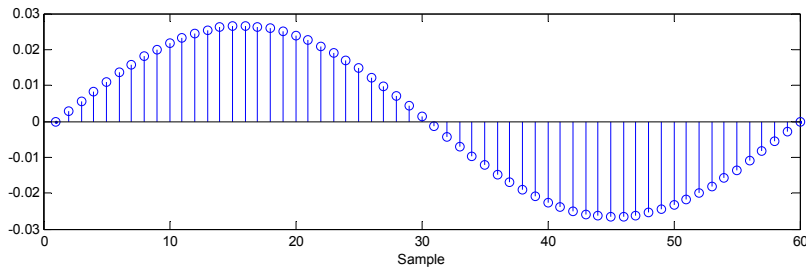


Fig. 4. Filter template.

The first target is a simple loop of 22 AWG copper wire formed into a loop with a circumference of 10 cm which has a theoretical relaxation frequency of 10.0 kHz. The loop is oriented so that its axis is z directed when the yaw and pitch angles are zero as shown on Figure 3b. The magnetic polarizability tensor of the loop is:

$$\mathbf{M}(\omega) = -\frac{\mu_0 A^2}{L} \left(\frac{j\omega/\zeta}{1+j\omega/\zeta} \right) \begin{bmatrix} 0 & 0 & 0 \\ 0 & 0 & 0 \\ 0 & 0 & 1 \end{bmatrix} \quad (1)$$

where $\zeta = 2\pi f_r$ is the relaxation frequency, A is the area of the loop and, L is the self inductance of the loop. The measured response for the single loop is presented in Figures 5, 6, and 7. In Figure 5a, the magnitude of imaginary part of the response is presented in pseudo-color graphs as a function of x and z at $y=0$ and $f=5,190$ Hz for five pitch angles and three yaw angles. For $pitch = 0^\circ$, the graphs are as expected; the strongest response is at $x = 0$, the response is symmetric about $x = 0$, and the response gets weaker as z increases. For $pitch = 22.5^\circ$, 45° , and 67.5° , the response is no longer symmetric about $x = 0$. For $pitch = 90^\circ$, the response is again symmetric about $x = 0$, but the maximum response is not at $x = 0$, and the response is almost zero when $yaw = 90^\circ$. In Figure 5b, the response computed from a theoretical model is shown which models the loop as an infinitesimal magnetic dipole with the magnetic polarizability tensor on equation 1. The theoretical results are very similar to the measured results.

In Figure 6, Argand diagrams of the response are presented from the experimental measurements and the theoretical model of the single-loop target at $x=0$, $y=0$, $z=4.5\text{cm}$ for three yaw and five pitch angles. The shape of the response is the same for all the rotation angles while the amplitude of the response changes with rotation angle. This is predicted theoretically since the loop only has a single relaxation.

In Figure 7, the discrete spectrum of relaxation frequencies⁸ of the response from experimental measurements and theoretical model of the single-loop target at $x=0$, $y=0$, $z=4.5\text{cm}$ for three yaw and five pitch angles. Here the data is fit to a relaxation (exponential) model, and the amplitude of each of the relaxation frequencies is plotted as a function of relaxation frequency. This analysis correctly identifies the 10 kHz relaxation frequency at all of the rotation angles except at $\text{pitch} = \text{yaw} = 90^\circ$ where the response is zero. The analysis also shows additional relaxations of very-low amplitude from the experimental data which may be due to secondary relaxations or noise.

The second target consists of three loops of copper wire that are at right angles to each other and is seen on Figure 3c. The magnetic polarizability tensor of the loops is:

$$\mathbf{M}(\omega) = -\frac{\mu_o A_x^2}{L_x} \left(\frac{j\omega/\zeta_x}{1+j\omega/\zeta_x} \right) \begin{bmatrix} 1 & 0 & 0 \\ 0 & 0 & 0 \\ 0 & 0 & 0 \end{bmatrix} - \frac{\mu_o A_y^2}{L_y} \left(\frac{j\omega/\zeta_y}{1+j\omega/\zeta_y} \right) \begin{bmatrix} 0 & 0 & 0 \\ 0 & 1 & 0 \\ 0 & 0 & 0 \end{bmatrix} - \frac{\mu_o A_z^2}{L_z} \left(\frac{j\omega/\zeta_z}{1+j\omega/\zeta_z} \right) \begin{bmatrix} 0 & 0 & 0 \\ 0 & 0 & 0 \\ 0 & 0 & 1 \end{bmatrix} \quad (2)$$

where $\zeta_k = 2\pi f_{rk}$ are the relaxation frequencies, A_k are the areas of the loops and, L_k are the self inductances of the loops with $k = x, y, z$. The parameters for the loops are presented in Table I.

Table I. Parameters for the three-loop target.

Orientation	Diameter (cm)	Wire Gauge (AWG)	Relaxation Freq. (kHz)
x	5	36	10.1
y	4	30	50.2
z	3	22	172

The measured and theoretical responses for the three-loop target are presented in Figures 8, 9, and 10. In Figure 8, the magnitude of imaginary part of the response is presented in pseudo-color graphs as a function of x and z at $y=0$ and $f=5,190\text{ Hz}$ for five pitch angles and three yaw angles. For $\text{pitch} = 0^\circ$ and 90° , the response should be symmetric about $x = 0$; however, the experimental results are slightly asymmetric for $\text{pitch} = 90^\circ$ which is probability due to the target being slightly out of alignment. Otherwise, the experimental and theoretical results are very similar. In Figure 9, Argand diagrams of the response are presented from the experimental measurements and the theoretical model. The shape and amplitude of the response now changes as a function of the rotation angles. This is predicted theoretically since the loop has a different relaxation frequency along each axis. This will make it more challenging to use the shape information for identification of such a complex target. In Figure 10, the discrete spectrum of relaxation frequencies of the response from experimental measurements and theoretical model of the three-loop target. This analysis correctly identifies the three relaxation frequencies of the target. Note the relative amplitude of the relaxations change as a function of the rotation angles. This representation of the data may be helpful for the discrimination of complex targets with unknown orientation.

The third target is a 9 mm shell casing, and its measurements are shown in Figures 11, 12, and 13. It is difficult to see that the response of this target varies with rotation angle from the graphs in Figures 11 and 12, however, the difference is apparent in the graphs in Figure 13. The discrete spectrum of relaxation frequencies for this target consist of three relaxations that have amplitudes that vary with the rotation angles as seen in Figure 13. The magnetic polarizability tensor for this target is unknown but these measurements contain sufficient data to construct it. We plan on deriving the magnetic polarizability tensor in future work.

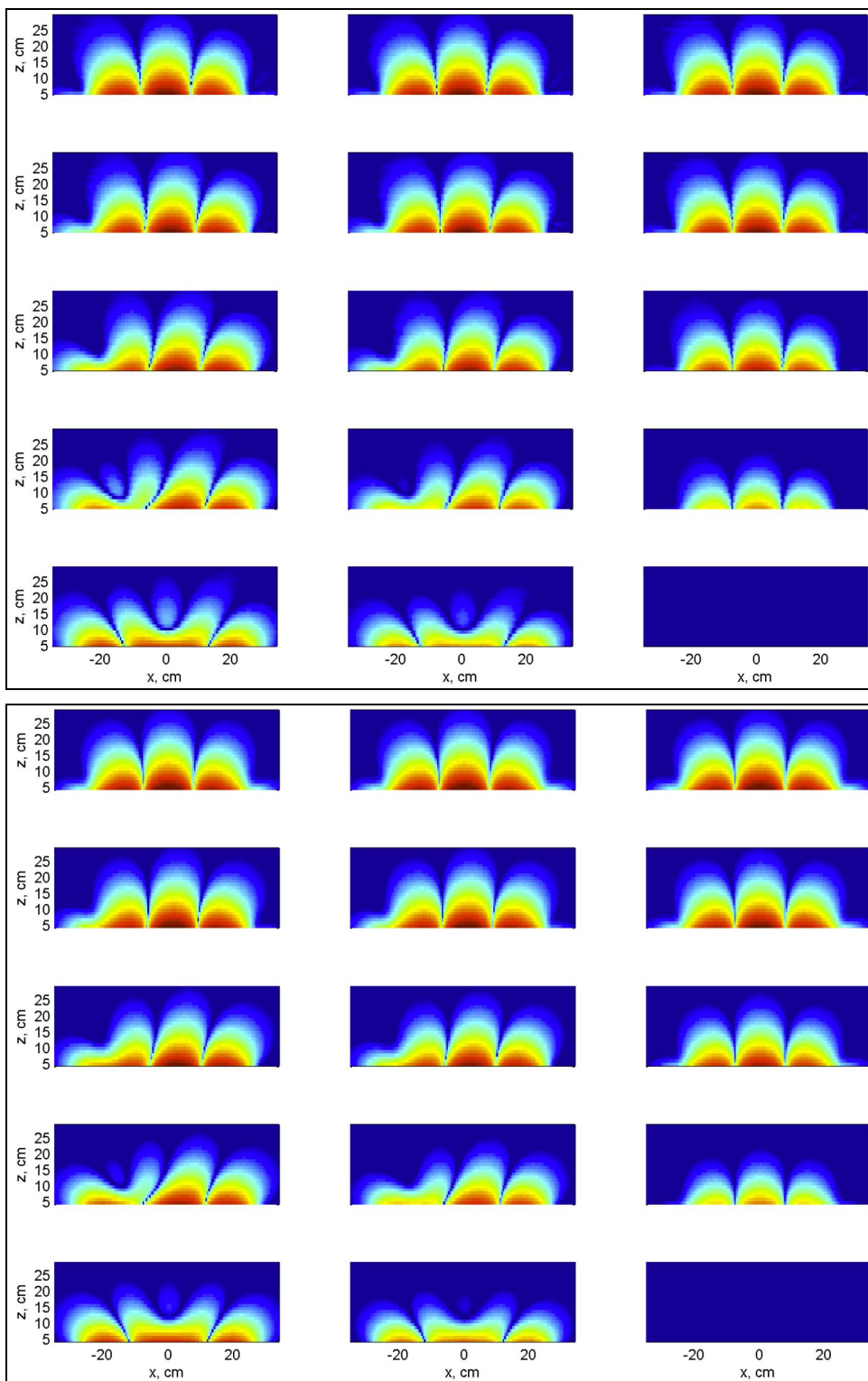


Fig. 5. Pseudo-color graphs of the magnitude of imaginary part of the response for the single-loop target from (a) experimental measurements and (b) theoretical modeling as a function of x and z at $y=0$ and $f=5,190$ Hz. The graphs are on a 60 dB scale using the Matlab jet color map. Pitch angles range from 0° to 90° in 22.5° increments from top to bottom. Yaw angles range from 0° to 90° in 45° increments from left to right in the figure.(color image in electronic version of manuscript)

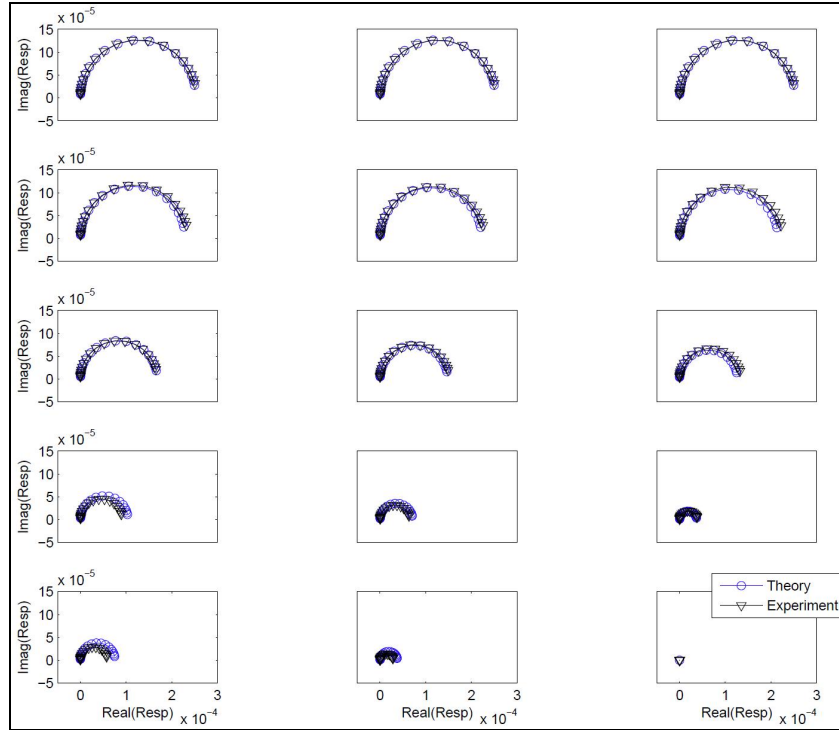


Fig. 6. Argand diagrams of the response from experimental measurements and theoretical modeling of the single-loop target at $x=0$, $y=0$, $z=4.5\text{cm}$ for three yaw and five pitch angles. Pitch angles range from 0° to 90° in 22.5° increments from top to bottom. Yaw angles range from 0° to 90° in 45° increments from left to right in the figure.

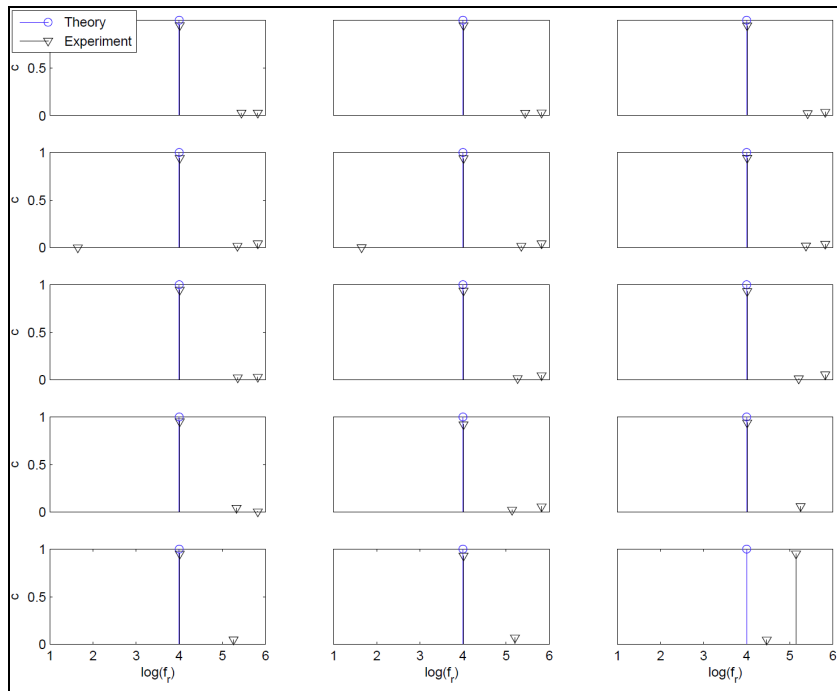


Fig. 7. Graphs of the discrete spectrum of relaxation frequencies of the response from experimental measurements and theoretical modeling of the single-loop target at $x=0$, $y=0$, $z=4.5\text{cm}$ for three yaw and five pitch angles. Pitch angles range from 0° to 90° in 22.5° increments from top to bottom. Yaw angles range from 0° to 90° in 45° increments from left to right in the figure.

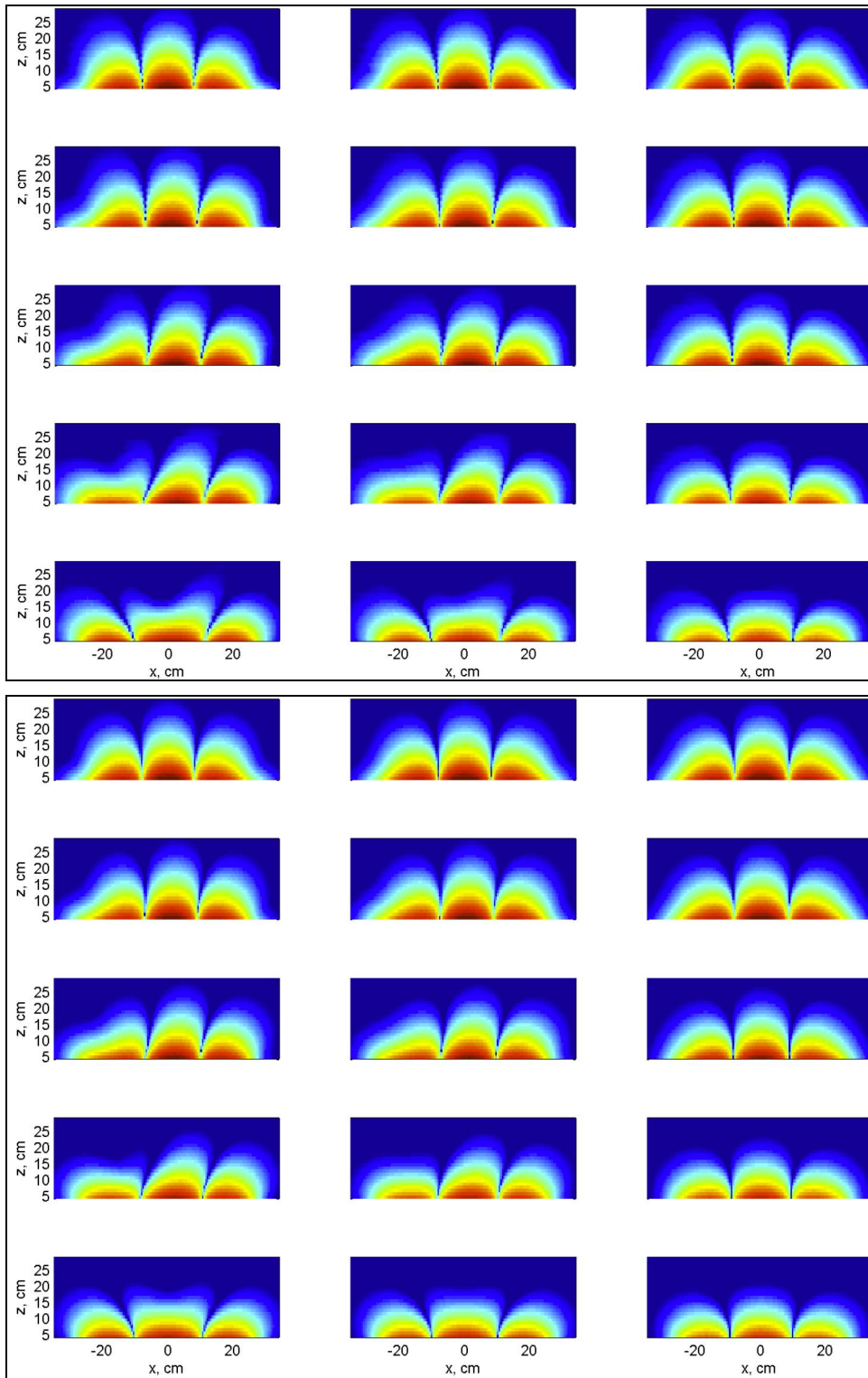


Fig. 8. Pseudo-color graphs of the magnitude of imaginary part of the response from (a) experimental measurements and (b) theoretical modeling for the three-loop target as a function of x and z at $y=0$ and $f=5,190$ Hz. The graphs are on a 60 dB scale using the Matlab jet color map. Pitch angles range from 0° to 90° in 22.5° increments from top to bottom. Yaw angles range from 0° to 90° in 45° increments from left to right in the figure. (color image in electronic version of manuscript)

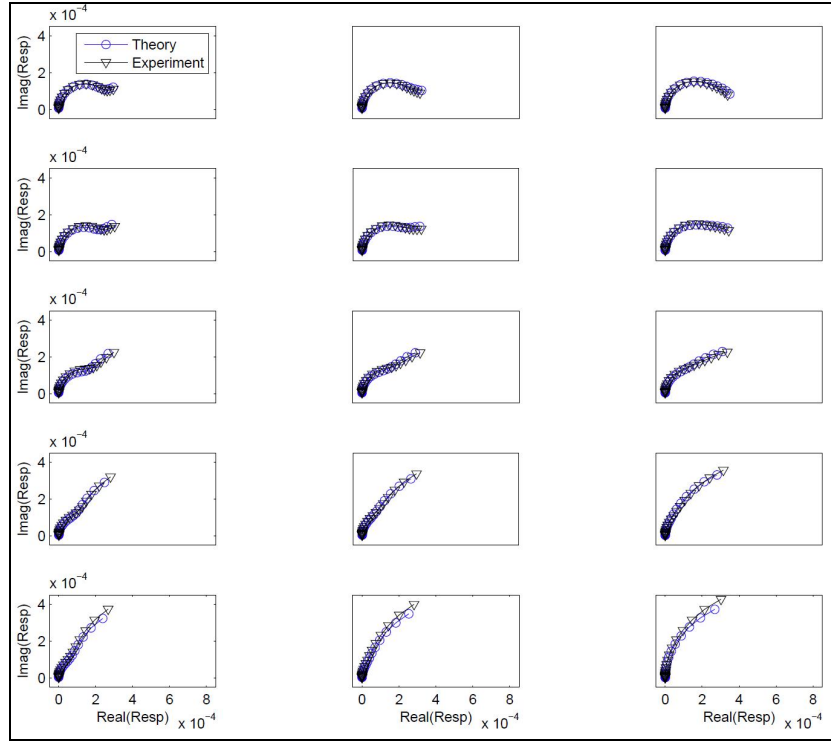


Fig. 9. Argand diagrams of the response from experimental measurements and theoretical modeling of the three-loop target at $x=0$, $y=0$, $z=4\text{cm}$ for three yaw and five pitch angles. Pitch angles range from 0° to 90° in 22.5° increments from top to bottom. Yaw angles range from 0° to 90° in 45° increments from left to right in the figure.

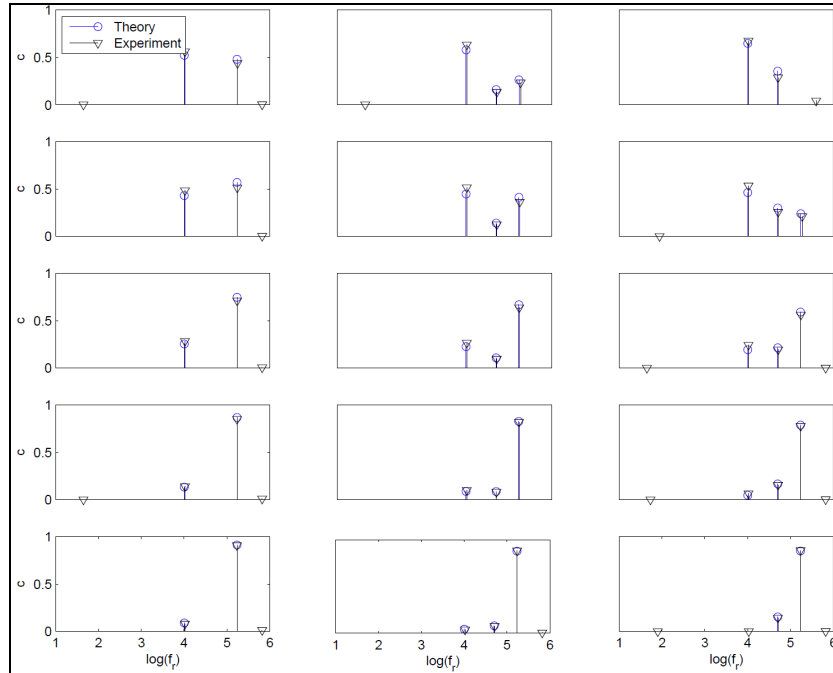


Fig. 10. Graphs of the discrete spectrum of relaxation frequencies of the response from experimental measurements and theoretical modeling of the three-loop target at $x=0$, $y=0$, $z=4\text{cm}$ for three yaw and five pitch angles. Pitch angles range from 0° to 90° in 22.5° increments from top to bottom. Yaw angles range from 0° to 90° in 45° increments from left to right in the figure.

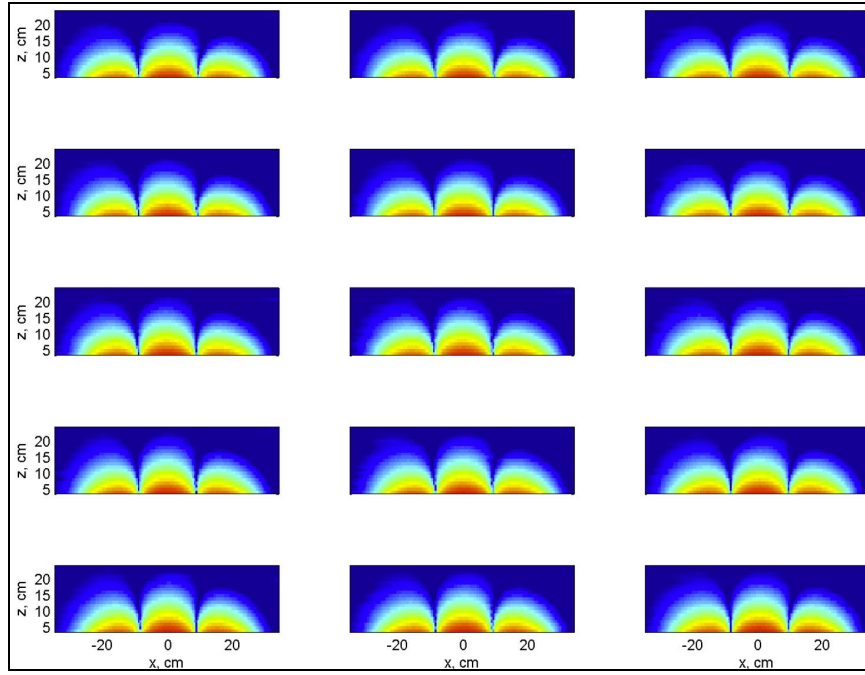


Fig. 11. Pseudo-color graphs of the magnitude of imaginary part of the response from experimental measurements of a 9 mm shell casing as a function of x and z at $y=0$ and $f=5, 190$ Hz. The graphs are on a 60 dB scale using the Matlab jet color map. Pitch angles range from 0° to 90° in 22.5° increments from top to bottom. Yaw angles range from 0° to 90° in 45° increments from left to right in the figure. (color image in electronic version of manuscript)

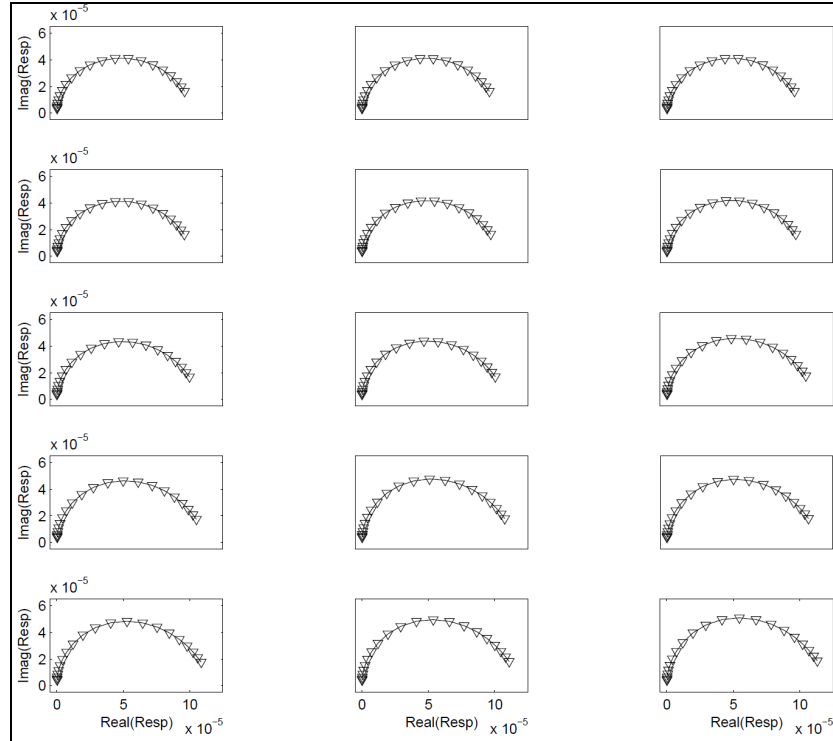


Fig. 12. Argand diagrams of the response from experimental measurements of a 9 mm shell casing at $x=0$, $y=0$, $z=3.2$ cm for three yaw and five pitch angles. Pitch angles range from 0° to 90° in 22.5° increments from top to bottom. Yaw angles range from 0° to 90° in 45° increments from left to right in the figure.

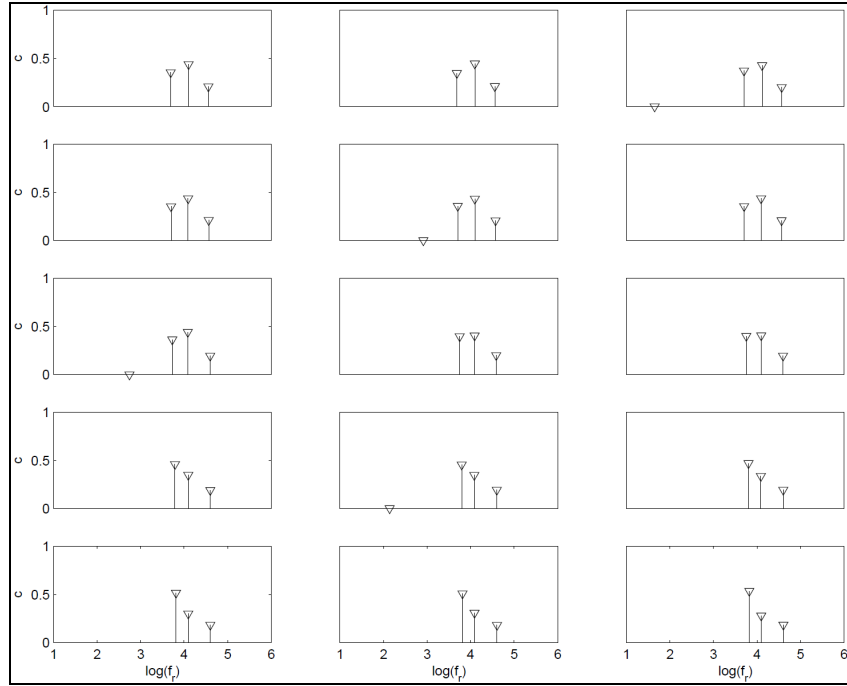


Fig. 13. Graphs of the discrete spectrum of relaxation frequencies of the response of a 9 mm shell casing at $x=0$, $y=0$, $z=3.2\text{cm}$ for three yaw and five pitch angles. Pitch angles range from 0° to 90° in 22.5° increments from top to bottom. Yaw angles range from 0° to 90° in 45° increments from left to right in the figure.

4. CONCLUSIONS

A new experimental facility has been established to measure the response of typical targets for EMI sensors as a function of location and orientation. This has been accomplished with a six-degree of freedom positioning system with five automated axes (the three translational axes and two rotational axes) and one manual axis. The EMI sensors are held fixed while targets are oriented using the rotational axes and then moved along a prescribed path through the measurement volume. Commercially available hardware has been used for the translational stages and one rotational stage while a custom-built rotational stage has been assembled to eliminate metal from the measurement region.

Measurements with this system provide a complete characterization of the targets for comparison to field measurements as well as with numerical modeling of EMI sensors for further hardware development. This type of data may also be used in the development of detection algorithms for EMI sensors. Future efforts with the experimental facility will include measurements of more targets and investigations of methods for summarizing the massive amounts of collected data into simple physical models. Further development of the processing algorithms will be done to help characterize more complicated targets and refine detection and discrimination methods for EMI sensors.

ACKNOWLEDGMENTS

This work is supported in part by the US Army Night Vision and Electronic Sensors Directorate, Science and Technology Division, Countermeasures Branch and in part by the U. S. Army Research Office under Contract Number W911NF-05-1-0257.

REFERENCES

1. Scott, W.R., Jr., "Broadband electromagnetic induction sensor for detecting buried landmines," *Proceedings of the 2007 IEEE Geoscience and Remote Sensing Symposium*, Barcelona, Spain, July 2007.
2. Scott, W. R., Jr., "Broadband Array of Electromagnetic Induction Sensors for Detecting Buried Landmines," IGARSS 2008, Vol. II, pp. 375-378.
3. P. Gao, L. Collins, P.M. Garber, N. Geng, and L. Carin, "Classification of Landmine-Like Metal Targets Using Wideband Electromagnetic Induction," *IEEE Transactions on Geoscience and Remote Sensing*, Vol. 38, No. 3, May 2000.

4. L. Collins, P. Gao, and L. Carin, "An Improved Bayesian Decision Theoretic Approach for Land Mine Detection," *IEEE Transactions on Geoscience and Remote Sensing*, Vol. 37, No. 2, March 1999.
5. G. D. Sower and S. P. Cave, "Detection and identification of mines from natural magnetic and electromagnetic resonances," in *Proc. SPIE*, Orlando, FL, 1995.
6. C. E. Baum, "Low Frequency Near-Field Magnetic Scattering from Highly, but Not Perfectly Conducting Bodies," Phillips Laboratory, *Interaction Note* 499, Nov. 1993.
7. E.B. Fails, P.A. Torrione, W. R. Scott, Jr, and L.M. Collins, "Performance of a four parameter model for modeling landmine signatures in frequency domain wideband electromagnetic induction detection systems," *Proceedings of the SPIE: 2007*, Vol. 6553, Orlando, FL, May 2007.
8. M. H. Wei, W. R. Scott, Jr., and J. H. McClellan, "Robust Estimation of The Discrete Spectrum of Relaxations for Electromagnetic Induction Responses," *submitted for publication in IEEE Transactions on Geoscience and Remote Sensing*.